HiSST: 2nd International Conference on
High-Speed Vehicle Science Technology
11–15 September 2022, Bruges, Belgium

Shock-Shock Interference Analysis for SpaceLiner Booster

L. Bussler[1], S. Karl[2], M. Sippel[3]

Abstract

The booster stage of SpaceLiner is a winged, reusable first stage launching vertically and landing horizontally. With a separation Mach number of around 13 at an altitude of approximately 70 km, it flies through regimes from hypersonic to subsonic along its descent trajectory. All of these flight regimes are relevant in the frame of the analysis of its design based on the occurring mechanical and thermal loads. One aspect present in the hypersonic flight regime and identified as potentially critical is the shock-shock interference. The shock wave originating at the fuselage nose hits the leading-edge of the wing and interferes with the wing leading-edge shock. This leads to a local increase in both pressure and heat flux within the region of shock-shock interference. The increased heat flux might go beyond thermal protection system limits and lead to severe damage of the reusable first stage. The primary objective of this paper is to quantify the heat flux increase due to shock-shock interference in the area of the wing leading-edge. Furthermore, to assess if the feasibility of SpaceLiner booster is put in question by the phenomenon of shock-shock interference. And finally, to determine whether fixed wing design options for SpaceLiner Booster are still viable despite shock-shock interference.

Keywords: *RLV, VTHL, Shock-Shock Interference, SpaceLiner*

Acronyms

AoA	Angle of Attack
CMC	Ceramic Matrix Composites
DLR	German Aerospace Center
FP	Flight Point
NPL	National Physical Laboratory
RLV	Reusable Launch Vehicle
SSI	Shock-Shock Interference
TSTO	Two-Stage-To-Orbit
VTHL	Vertical Take-Off Horizontal Landing

Nomenclature

c	-	Heat Capacity	[J/kg K]
k	-	Thermal Conductivity	[W/m K]
q̇	-	Heat Flux	[W/m²]
R	-	Leading-Edge Radius	[m]
T	-	Temperature	[K]
t	-	Time	[s]
ρ	-	Density	[kg/m³]
ε	-	Surface Emissivity	[-]
Λ	-	Leading-Edge Sweep Angle	[°]

[1] *DLR Institute of Space Systems, SART, Bremen Germany, Leonid.Bussler@dlr.de*
[2] *DLR Institute of Aerodynamics and Flow Technology, Goettingen Germany, Sebastian.Karl@dlr.de*
[3] *DLR Institute of Space Systems, SART, Bremen Germany, Martin.Sippel@dlr.de*

1. Introduction

The SpaceLiner concept is a fully reusable vertical take-off horizontal landing (VTHL) configuration, [1] - [3]. The two-stage system is primarily designed for civil, hypersonic intercontinental passenger transport with the ultimate goal of achieving a flight time of around 90 minutes for a connection between Europe and Australia. A two-stage-to-orbit (TSTO) variant derived from the passenger configuration is also under consideration, [2]. The analysis of further variants is ongoing, [4], [5]. The SpaceLiner system consists of two rocket-propelled, winged stages consuming liquid hydrogen as fuel and liquid oxygen as oxidizer. After vertical take-off and mated ascent, the separation of the booster stage takes place at Ma 12.6 at an altitude of 69 km. The second stage continues to accelerate to reach velocities just below orbital. This allows reaching the target destination by performing an unpowered, long-distance gliding flight. In contrast to that, the booster stage performs an unpowered reentry into the atmosphere and returns to launch site for a horizontal landing. The ascent configuration of SpaceLiner is shown in Fig 1, [1].

Fig 1. SpaceLiner ascent configuration, [1]

In this paper the focus is on the first stage of the SpaceLiner configuration. An overview of the SpaceLiner booster stage and a presentation of its reference descent trajectory is given in section 2. The booster stage is of utmost importance for successfully performing the SpaceLiner mission. It contains the majority of the propellant, is cross-feeding the second stage and is providing over 80 % of the thrust at lift-off. Being a winged first stage, it is able to achieve an efficient atmospheric reentry with moderate mechanical and thermal loads. However, the requirement of flying through a wide range of Mach numbers and altitudes places constraints on the SpaceLiner booster outer shape and like many delta wing configurations with varying leading-edge sweep, the SpaceLiner first stage encounters the problem of shock-shock interference (SSI) in the area of the outer wing leading-edge. At certain flight conditions the nose shock wave may interfere with the shock wave that develops at the wing leading-edge and this can lead to both higher pressure and heat flux loads. The latter being of special interest from a thermal protection system point of view.

The main objective of this paper is to quantify the heat flux increase due to SSI on the leading-edge of the SpaceLiner booster wing. To prepare the analysis of heat flux, in section 3 an estimation of the leading-edge surface temperature is presented using an empirical heat flux formulation. While for the wing leading-edge region outside of the nose bow shock such empirical relationships and also simplified computational methods do exist, this is not the case for the leading-edge region where the complex phenomenon of SSI takes place. The heat flux increase depends on the particular geometry of the vehicle, the flight conditions and the resulting shock geometry and needs to be taken into consideration already at an early stage of the design process. Thus, within the presented work both inviscid and for the first time also viscous CFD is performed for the SpaceLiner booster stage. They are presented in

section 4. Inviscid calculations are performed for a wider range of supersonic and hypersonic Mach numbers and focus on a first visualization of the shock geometry and the aerodynamics of the SpaceLiner booster stage. Viscous CFD is performed in a narrower Mach range around the heat flux maximum along the reference descent trajectory and allows the determination of the increased heat flux levels in the area of the leading-edge due to SSI. The RANS simulations are performed for an isothermal wall condition at two different specified wall temperatures to allow recalculation of heat flux results for alternative, estimated wall temperatures.

2. SpaceLiner Booster Stage

2.1. Design of SpaceLiner Booster Stage

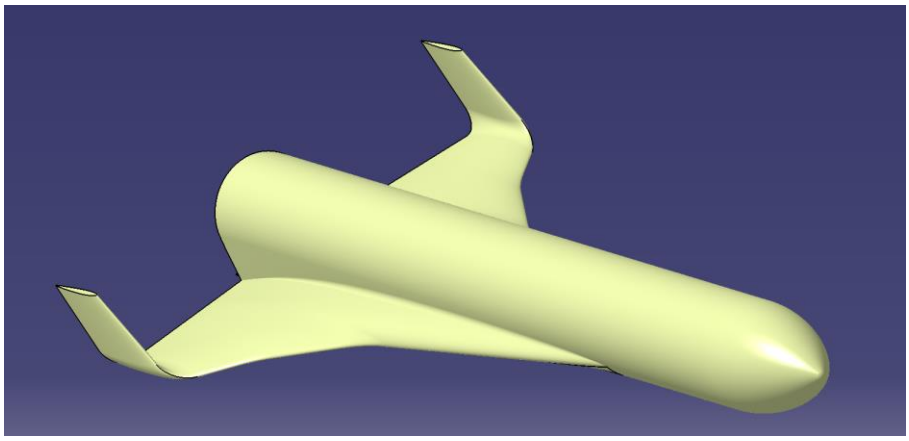

Fig 2. Fixed wing design, SpaceLiner 7-3 booster stage

In this paper the SpaceLiner 7-3 booster stage shown in Fig 2 is analyzed. It is basically a wing-fuselage combination with vertical stabilizers at the tips of the wing. The fixed wing of the stage is a triple-delta wing with leading-edges swept at 82°, 61° and 43°. The following airfoil sections are used to define the wing geometry:

- Root of the wing: NPL-EC/ECH 4.5 with a leading-edge radius of 55 mm
- Inner mid position at 44 % semi-span: NPL-EC/ECH 7.0 with a leading-edge radius of 60 mm
- Outer mid position at 72 % semi-span: NPL-EC/ECH 8.0 with a leading-edge radius of 60 mm
- Tip of the wing: NPL-EC/ECH 10.0 with a leading-edge radius of 70 mm

Additional details on the design of the SpaceLiner booster stage wing can be found in [1]. The outer dimensions of the stage are given in Fig 3. The stage is 80.5 m long, has a wingspan of 36.1 m and a fuselage diameter of 8.6 m. The radius of the fuselage nose is 0.5 m.

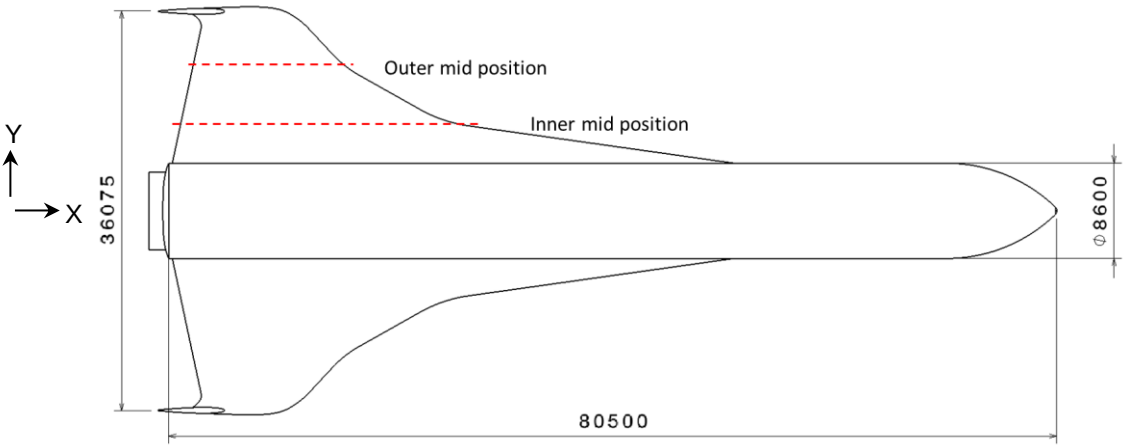

Fig 3. SpaceLiner 7-3 booster stage outer dimensions (mm)

Looking at the potential difficulties associated with shock-shock interference for fixed wing design concepts, recently a booster stage variant with a variable outer wing has been proposed, [6]. The variable wing design of the SpaceLiner booster stage is shown in Fig 4. The idea of this proposal is to avoid shock-shock interference in the supersonic and hypersonic flight regimes by folding the outer wing segments into the inner wing (Fig 4 left). This is motivated by the fact that in hypersonic flight neither a large wing area nor a high lift-to-drag ratio is required. The main objective for the SpaceLiner booster stage is an aerodynamically trimmed and safe reentry flight. For subsonic flight the outer wing segments are unfolded and contribute to increasing the lift and lift-to-drag ratio of the SpaceLiner booster stage (Fig 4 right).

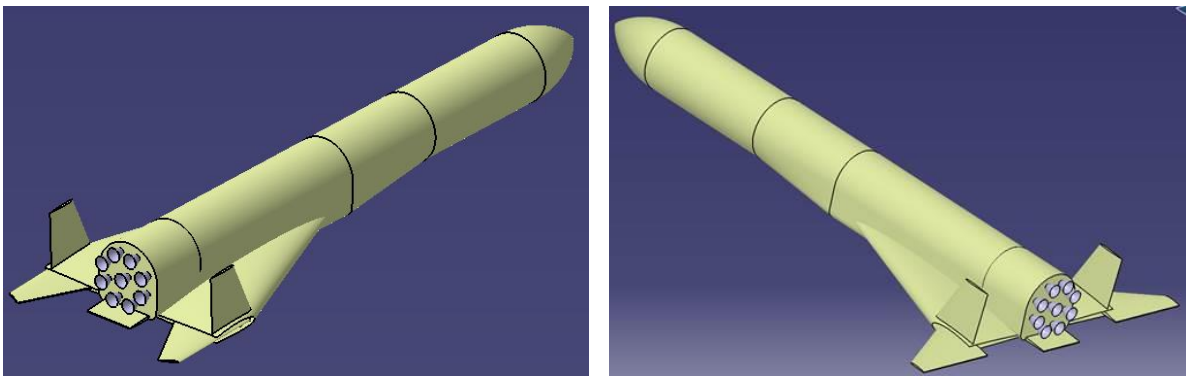

Fig 4. Variable wing design for SpaceLiner booster stage, [6]

It is clear that while potentially avoiding the occurrence of shock-shock interference this design option does increase amongst others the mass and in general the complexity of the wing and overall stage design. Thus, this raises the question of justifying the massive design adaptation. This sort of adaptation would only be required if heat loads and temperatures would go beyond the limits of available thermal protections system materials. To decide on this design trade-off, it is a must to determine how dangerous and severe the heat flux increase coming from SSI is. This is one of the objectives of the presented work.

2.2. SpaceLiner Booster Reference Descent Trajectory

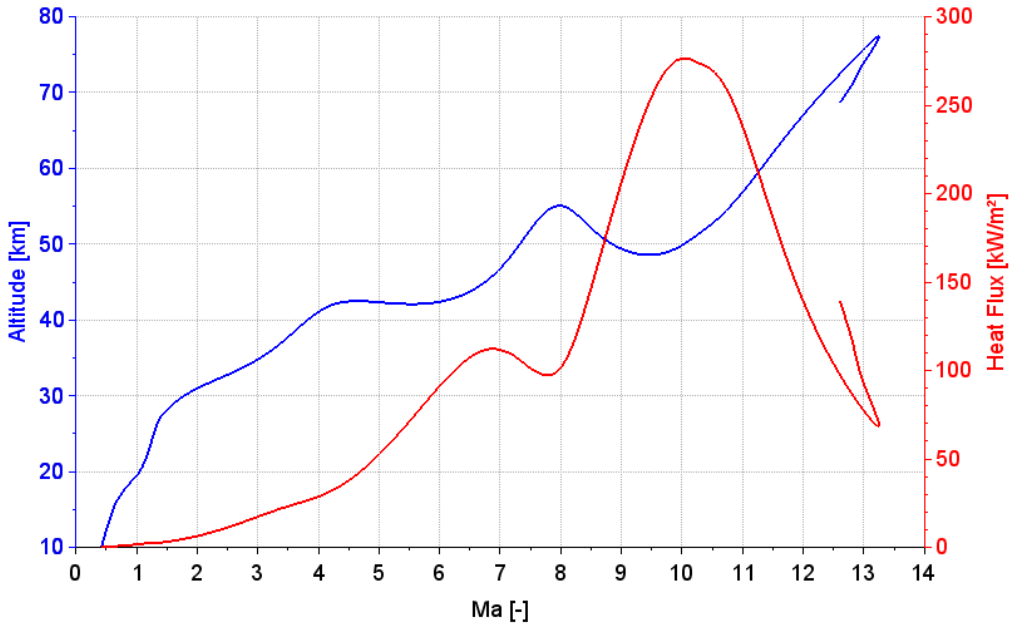

Fig 5. Reference descent trajectory of SpaceLiner Booster, [8]

The descent trajectory used within the presented analysis is the result of a 4 degree of freedom simulation. It is using a hybrid aerodynamic database containing aerodynamic coefficients obtained

with inviscid CFD, hypersonic and super-/subsonic panel methods as well as semi-empirical methods, see [7]. The reference descent trajectory of the SpaceLiner booster stage is shown in Fig 5, [8]. Altitude and nose stagnation point heat flux are displayed over the freestream Mach number. The heat flux is an empirically estimated cold wall heat flux. The separation of the booster stage takes place at Ma 12.6 at an altitude of 69 km. After reaching a maximum altitude of more than 77 km the winged reusable stage having a mass of 193 Mg reenters the atmosphere. It faces a maximum nose stagnation point heat flux of more than 275 kW/m² at a Mach number of 10.0 at an altitude of approximately 50 km. Following a skip out a second local heat flux peak is occurring at roughly Ma 7.0 and 45 km altitude.

3. Estimation of Surface Temperature

Table 1. Material properties of generic CMC

ρ [kg/m³]	ε [-]	c [J/kg K]	k [W/m K]	T [K]
2000	0.83	1398	15.4	800

The determination of heat fluxes based on viscous CFD calculations does require information about the temperature of the surface. In the analysis presented we are concerned about the wing leading-edge heat fluxes in the area of SSI. Thus, an estimation of the surface temperature is performed for the outer wing leading-edge of the SpaceLiner booster stage. The estimated temperature is used as input for the calculation of heat flux based on viscous CFD results.

The surface temperature estimation relies on modeling the heating as a transient heat conduction problem. Thus, the starting point is the one-dimensional partial differential equation of heat conduction without heat generation:

$$\frac{\rho\, c}{k}\,\frac{\partial T}{\partial t} - \frac{\partial^2 T}{\partial x^2} = 0 \tag{1}$$

In the above equation ρ is the density of the material, c its heat capacity, k its thermal conductivity, T the surface temperature, t the time and x the 1-D coordinate. Further, a semi-infinite body is assumed. For the boundary condition of constant surface heat flux, one has the following solution for the surface temperature, [9]:

$$T(t, \dot{q}) = T_0 + 2\,\dot{q}\,\sqrt{\frac{t}{\pi\,\rho\,c\,k}} \tag{2}$$

Here $\dot{q}$ is the surface heat flux and T_0 is the initial temperature. Since ceramic matrix composites (CMC) are one potential candidate for the leading-edge material, a generic CMC material is defined and its temperature dependent heat capacity and thermal conductivity are used to determine the surface temperature evolution. The properties of the generic CMC material with heat capacity and heat conductivity at a temperature of 800 K are shown in Table 1. The density of the material is set to be 2000 kg/m³, while the surface emissivity is assumed to be 0.83. The chosen and assumed values of the generic CMC material are oriented upon typical values for this group of materials, see e.g. [10]. Using the defined material properties, the evolution of surface temperature over time is derived by superposing the solutions of the one-dimensional heat conduction differential equation for the boundary condition of constant surface heat flux. Starting from an initial temperature the solutions are calculated for different incremental times and heat fluxes and summed to obtain the surface temperature at a specific point in time.

To be able to derive the evolution of temperature along the descent trajectory an empirical relationship for the leading-edge heat flux outside the nose bow shock is used. This relationship was used in the frame of Space Shuttle preflight analysis, [11]:

$$\dot{q}_{LE} = \dot{q}_{REF}\,\frac{1}{\sqrt{2}}\,\sqrt{\frac{R_{REF}}{R}}\,cos^{1.2}\Lambda \tag{3}$$

It is connecting the swept leading-edge heat flux $\dot{q}_{LE}$ to the heat flux $\dot{q}_{REF}$ on a sphere with a radius R_{REF} of 1 ft and considering leading-edge radius R and sweep angle Λ. For both the radius and sweep

angle of the leading-edge effective values are defined that do consider geometric sweep and radius as well as the effect of angle of attack, more details can be found in [11]. This equation is applicable to regions outside the nose bow shock and is applied to the outer segment of the SpaceLiner booster triple delta wing. The geometric leading-edge sweep angle and radius used for the presented analysis are 43° and 0.065 m respectively. The reference heat flux $\dot{q}_{REF}$ is calculated with a stagnation point heat flux relationship for spheres, [12]. The relationships for spheres and leading-edges discussed so far would represent cold wall heat fluxes. For the presented analysis the radiation of the surface is considered (surface emissivity shown in Table 1) and a hot wall correction is performed.

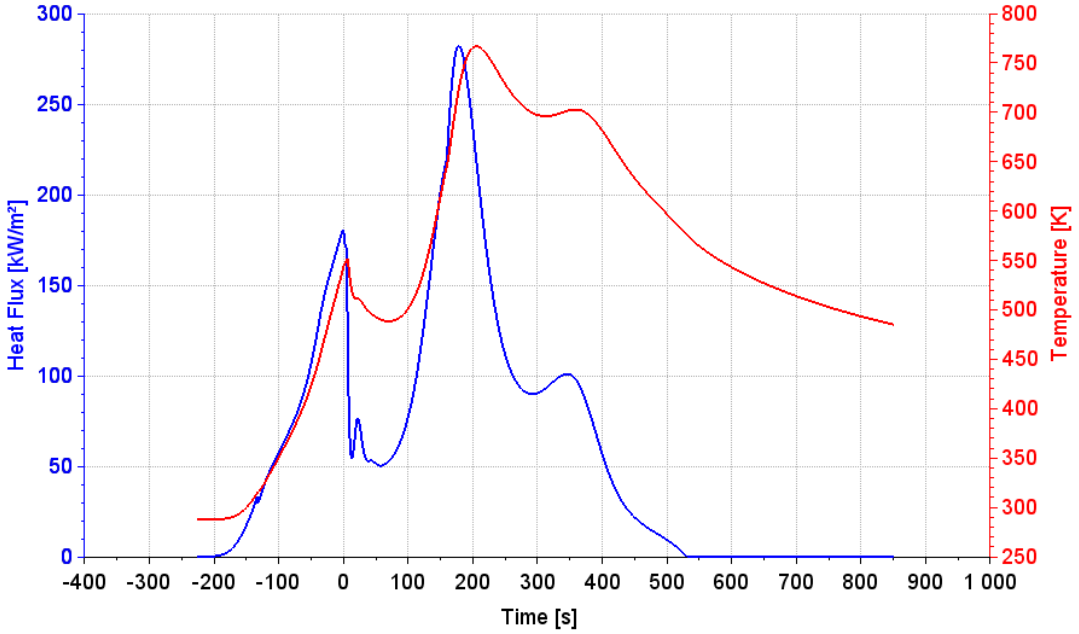

Fig 6. SpaceLiner booster wing empirical leading-edge heat flux and temperature

For the evolution of surface temperature not only the descent trajectory but also the ascent flight path plays a role. The heat load experienced during the ascent does as well contribute to the wing leading-edge temperature rise. Thus, for the estimation of temperature evolution, both the ascent and descent trajectories of the SpaceLiner booster stage are considered. The leading-edge heat flux obtained for the SpaceLiner booster stage along its ascent and descent trajectories is shown in Fig 6 together with the surface temperature estimation based on one-dimensional heat conduction. Heat flux and temperature are shown over time of flight, with 0 s indicating booster stage separation, thus showing negative times for the ascent phase. At the end of the ascent a heat flux of around 180 kW/m² is achieved. After a heat load decrease following stage separation, the heat flux rises again at the begin of atmospheric reentry and a maximum value of approximately 280 kW/m² is reached. A second, local heat flux peak of around 100 kW/m² is present around 350 s into the reentry. The resulting temperature evolution shows values of around 540 K at the end of the ascent phase, maximum values of 770 and 700 K during the peak heating phase and decreases to values below 500 K at the end of the descent flight.

4. CFD Calculations

4.1. Inviscid Calculations

In the frame of the presented analysis inviscid calculations are performed for free stream Mach numbers of Ma 3.0 to Ma 13.0 at a Ma 2.0 step for angle of attacks oriented at the SpaceLiner booster reference descent trajectory. The calculations are performed using OpenFOAM's sonicFoam solver on a hex-dominant mesh of 2.5 M elements. Perfect gas with a ratio of specific heats of 1.4 is used as gas model. The focus of the inviscid calculations is a first visualization of the shock geometry and the aerodynamics of the SpaceLiner booster stage. The Mach number distributions for free stream Mach numbers of Ma 3.0 at 25° AoA and Ma 13.0 at 40° AoA are shown in Fig 7.

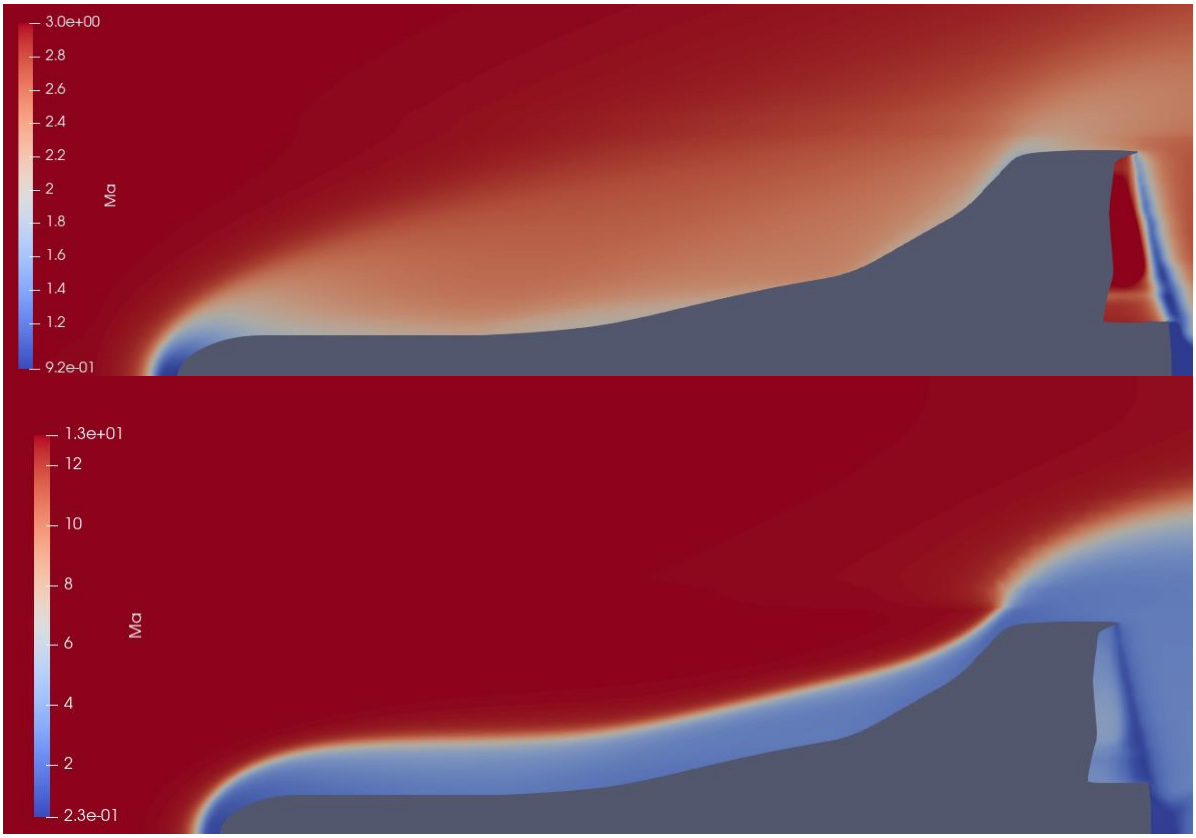

Fig 7. Mach distributions Ma 3.0 / AoA 25° (top), Ma 13.0 / AoA 40° (bottom)

While at Ma 3.0 the nose shock is rather weak and clearly not interfering with the wing leading-edge, at Ma 13.0 the nose bow shock is much more pronounced and closer to the geometry of the SpaceLiner booster stage. However, due to the fact that the gas model is calorically perfect gas with a constant ratio of specific heats of 1.4, the shock standoff distances can be expected to be overestimated.

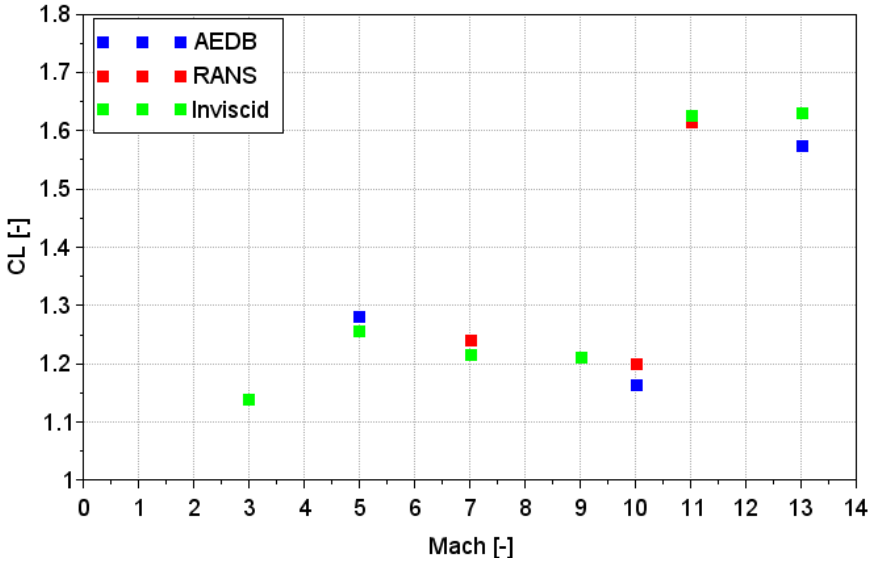

Fig 8. SpaceLiner booster lift coefficient

Since the problem of shock-shock interference cannot be addressed adequately by inviscid CFD with a calorically perfect gas, viscous calculations with an equilibrium gas model are performed and presented in section 4.2. Another aspect that is of interest from a systems analysis point of view is the aerodynamics of the SpaceLiner booster stage. The flight points later selected for viscous CFD analysis are based upon the reference descent trajectory that was obtained using a hybrid aerodynamic database composed out of different sources, [7]. Now with additional aerodynamic data obtained within

the frame of the presented work, a comparison of these inviscid and viscous RANS data with the hybrid aerodynamic database (AEDB) used for the calculation of the reference descent trajectory can be done.

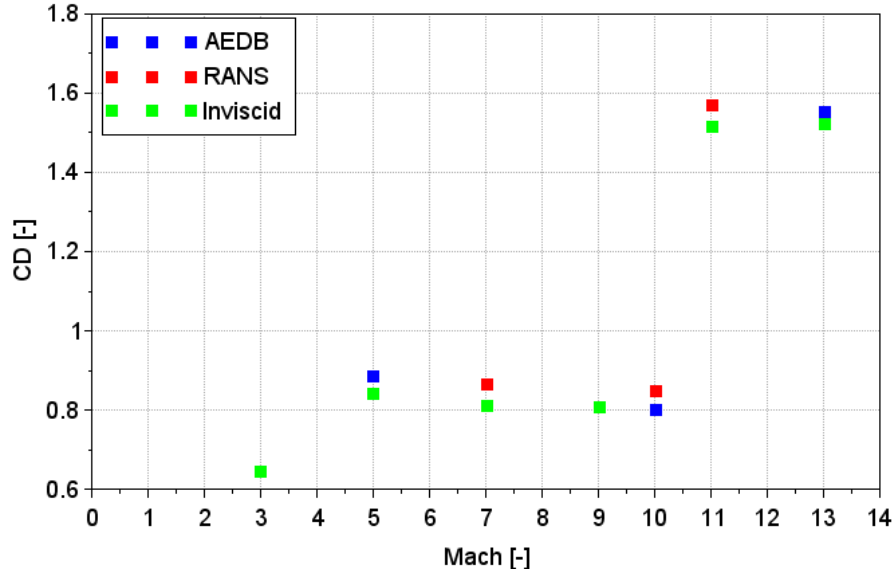

Fig 9. SpaceLiner booster drag coefficient

The reference area used to nondimensionalize the aerodynamic forces is 461 m². Results are presented for a Mach number range from Ma 3.0 to Ma 13.0. The angle of attack for Ma 3.0 is 25°, for Ma 5.0 to 10.0 it is 30° and Ma 11.0 and 13.0 it is 40°. The lift coefficient of the SpaceLiner booster stage over Mach number is shown in Fig 8, the drag coefficient in Fig 9. It should be noted that the data presented applies to the clean configuration only. Flap deflections are not considered. Looking at the relative deviations between the different sources of information for the lift and drag coefficients one can observe a maximum relative difference of 3.5 % for the lift coefficient and 6.1 % for the drag coefficient. While a detailed comparison of the different sets of aerodynamic data is not in the scope of the presented work, the good agreement of aerodynamic data from different sources does demonstrate consistency in the SpaceLiner booster stage design and supports the justification of the flight points selection for viscous CFD analysis.

4.2. SpaceLiner Booster SSI Effects on Leading-Edge Heat Flux Analyzed by RANS

Table 2. Selected flight points for viscous CFD analysis

FP	Ma [-]	AoA [°]	Alt [km]	T_{wall} [K]
1	11	40	60	595
2	10	30	50	700
3	7	30	45	700

The viscous CFD simulations are performed with the DLR Navier-Stokes solver TAU [13]. The computational domain comprises a half-configuration. The spatial discretization is based on an unstructured grid topology with 4.4M control volumes. Boundary layers are meshed with prismatic layers and a dimensionless wall spacing of the first layer of y+ in the order of unity was ensured to provide accurate resolution for the applied Spalart-Allmaras turbulence model [14] in low-Reynolds formulation. Large grid density was applied in the near body and shock interaction regions. The high temperature air properties are computed from a 11-species air model assuming chemical equilibrium. The thermodynamic properties of the individual species are computed from partition functions which accurately describe vibrational and electronic excitation and anharmonicity effects [15]. Walls are modelled using an isothermal condition. Parametric sets of computations at different wall temperatures are performed to quantify the effect on the local heat flux distribution.

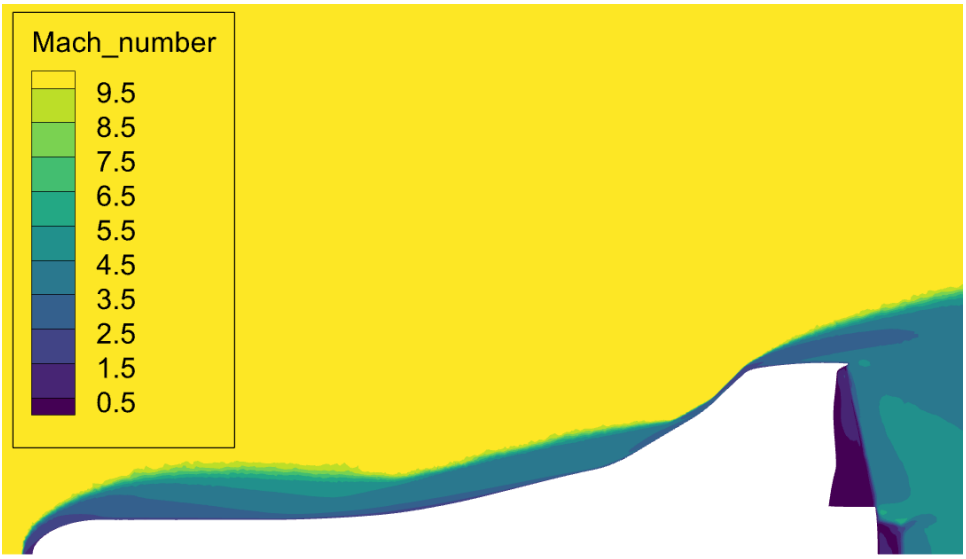

Fig 10. Mach distribution and shock geometry at FP 2 (Ma=10 / AoA=30° / Alt=50 km)

The flight points selected for viscous CFD analysis are chosen based on the reference descent trajectory in the vicinity of heat flux peaks and are summarized in Table 2, also showing the estimated wall temperature. The RANS calculations are performed for two different wall temperatures per flight point with a difference of 100 K. Calculations for flight point one and three are done at 750 and 850 K, for flight point two at 800 and 900 K. This does allow to obtain the dependency of heat flux results on surface temperature and to adapt the results to the surface temperature estimate at a certain flight point.

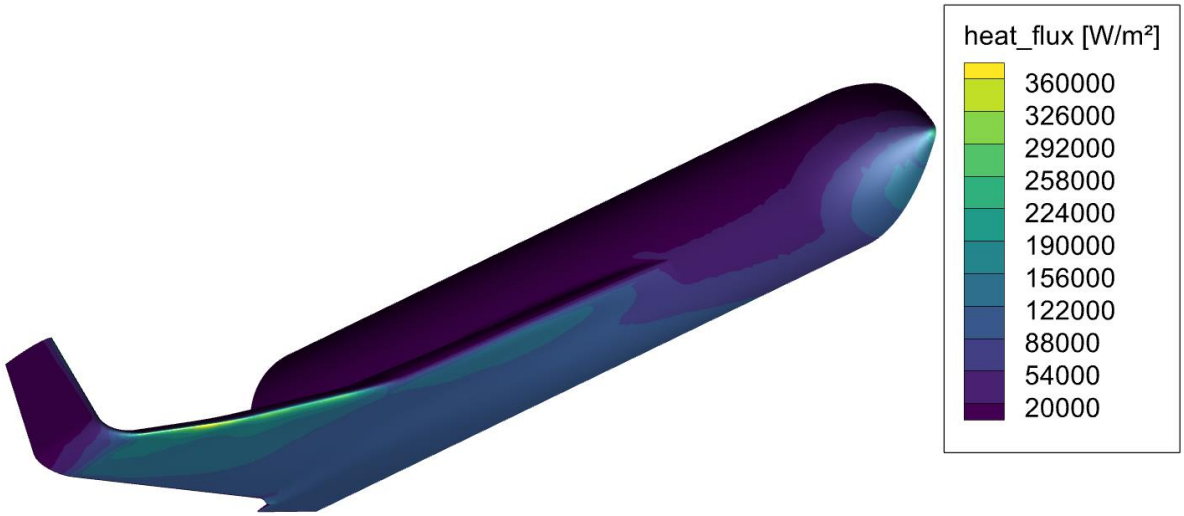

Fig 11. Heat flux distribution at FP 2 (Ma=10 / AoA=30° / Alt=50 km)

Illustrative results from the CFD analysis of the flow field around the booster configuration at trajectory flight point 2 at a wall temperature of 900 K are shown in Fig 10 and Fig 11. The interaction of the vehicle bow shock with the outboard wing is visible in the Mach number contours on the vehicle planform in Fig 10. The resulting heat flux peak of around 360 kW/m² is visible in Fig 11 on the wing leading-edge. The shock interference zone together with the small leading-edge radius result in a distinct region of peak thermal loading at the outboard wing and imposes the sizing constraint for the thermal protection system.

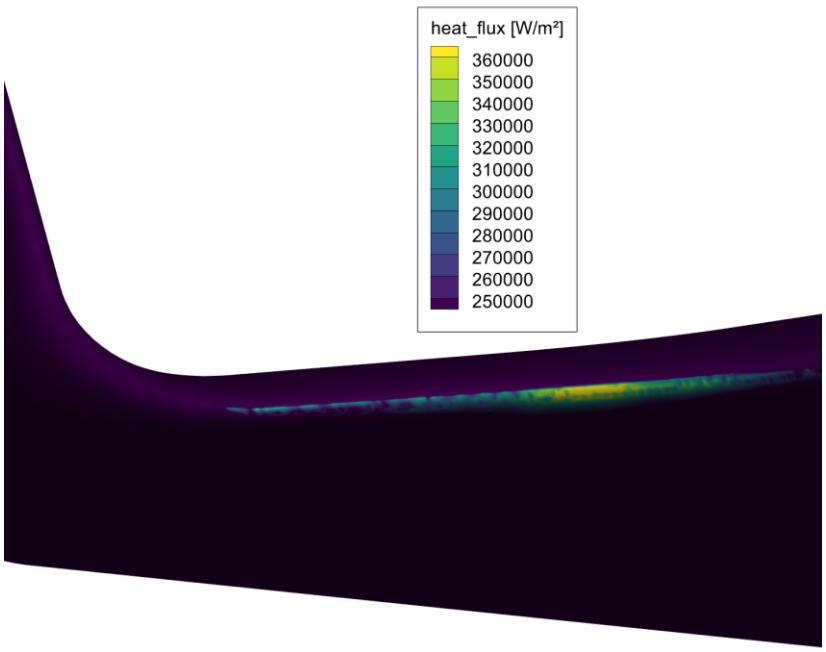

Fig 12. Heat flux distribution – zoomed into the area of SSI at FP 2 (Ma=10 / AoA=30° / Alt=50 km)

Note the reduced shock layer thickness in Fig 10 as compared to Fig 7(bottom). This effect is due to the application of different thermo-chemical models. The results in Fig 7 are obtained with a calorically perfect gas assumption and the RANS computations in Fig 10 are based on equilibrium air chemistry including high temperature thermodynamics of the gas species. This reduces the shock layer temperature due to vibrational excitation of the molecules and endothermal chemical reactions which results in an increased shock layer density and reduced shock standoff distance. These results highlight the importance of adequate thermo-chemical modelling of the shock layer gas to predict the correct spatial location of the interaction zones along the leading-edge.

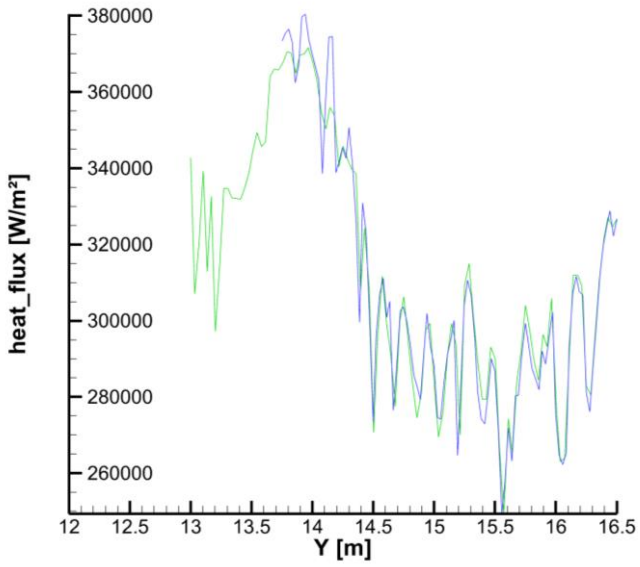

Fig 13. Heat flux distribution along leading-edge sampled along two precise lines for FP 2

As can be seen in Fig 12 the heat flux peaks occurring in the area of the leading-edge are limited to a narrow area at the very front of the outboard leading-edge. Above and below the heat flux level decreases quickly. Also, there is a certain variation in the level of heat flux along the spanwise direction (Y - measured from fuselage centerline outward). This is shown in Fig 13 for two straight lines defined

along the outer wing leading-edge. Depending on the definition of the line there is a slight variation in both the level of heat flux as well as the position of the local heat flux maxima. Despite of these variations, from a system design point of view the maximum heat flux as a function of the spanwise coordinate is of special interest, even if the points of maximum heat flux are not found precisely on the same line. Thus, in the following peak heat flux results at outboard wing span stations are presented. The objectives are to show the evolution of maximum leading-edge heat flux over the outboard wing segment and to determine the increase in heat flux due to shock-shock interference. Furthermore, to compare the calculated level of heat flux on the outer leading-edge with values obtained with the empirical relationship presented above as well as with the DLR in-house preliminary analysis aerothermodynamics tool HOTSOSE, [16].

The RANS heat flux trends shown in Fig 14 to Fig 16 are adapted to the estimated wall temperature from Table 2 using the heat flux gradient obtained by performing the RANS calculations for two different wall temperatures. HOTSOSE calculations are as well performed for the estimated wall temperatures shown in Table 2. This is also the case for the results of the empirical leading-edge heat flux relationship. As shown in Fig 10 the interference of the shock wave originating at the nose of the stage and the wing occurs in the area of the outer wing segment with a leading-edge sweep of 43°. This region is in the range from 72 % to 91 % relative semi-span. The RANS leading-edge heat flux evolutions shown in Fig 14 to Fig 16 are thus displayed for this semi-span range in steps of 0.25 m. For the empirical relationship and the HOTSOSE tool only results outside the region of SSI are shown. This is due to the fact that neither the empirical formula nor the HOTSOSE program are applicable in the region of SSI. Here two points at 86 % and 91 % semi-span are calculated for each flight point. They define the lines shown for the empirical relationship and HOTSOSE in Fig 14 to Fig 16.

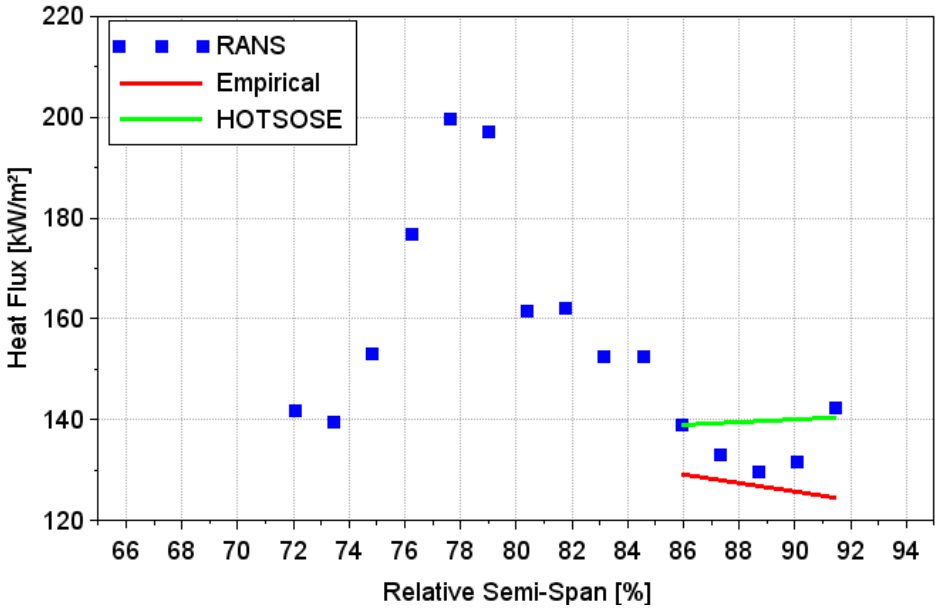

Fig 14. Heat flux evolution at FP 1 (Ma=11 / AoA=40° / Alt=60 km)

The heat flux evolution over the outboard wing leading-edge for flight point 1 is shown in Fig 14. The maximum leading-edge heat flux reaches a value of almost 200 kW/m² at approximately 78 % relative semi-span. Following the leading-edge in outward direction the heat flux does decrease down to around 130 kW/m² at 90 % semi-span. For the RANS results the heat flux ratio between the maximum heat flux and the one at 90 % semi-span is approximately 1.5, while the empirically estimated trend yields values of 129 kW/m² to 125 kW/m². HOTSOSE results are almost constant at around 140 kW/m². The slight decrease of the empirical results can be explained by a small increase in leading-edge radius. For flight point 1 there is a distinct heat flux increase in the area of SSI. Outside the region of SSI, the maximum relative difference between RANS, Empirical and HOTSOSE results is around just 12 %.

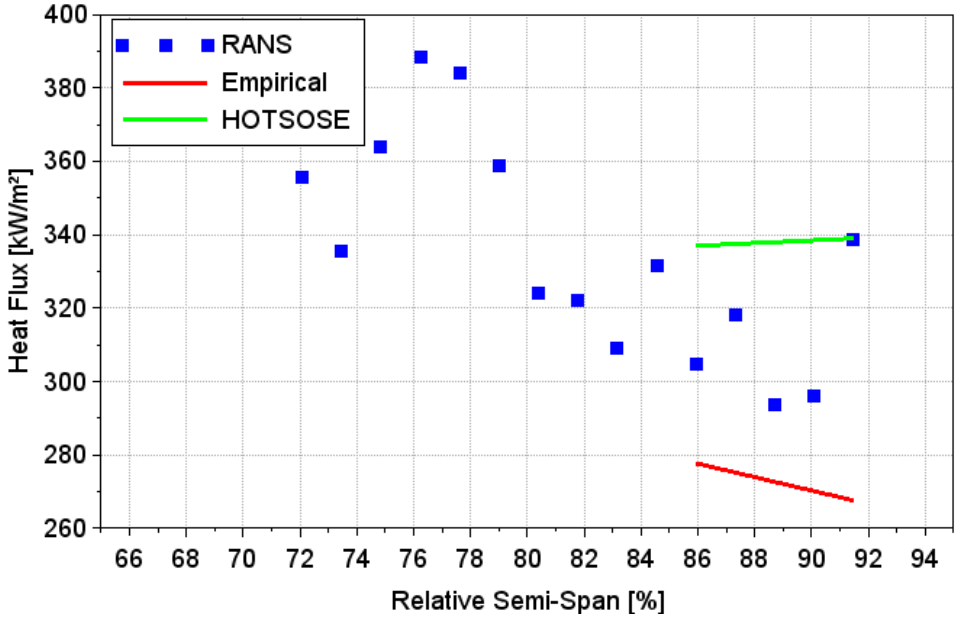

Fig 15. Heat flux evolution at FP 2 (Ma=10 / AoA=30° / Alt=50 km)

For flight point 2 at Ma 10.0 the heat flux increase due to shock-shock interference is less pronounced and the ratio between maximum and outboard heat flux decreases to 1.3, see Fig 15. Also, outside the region of SSI the amplitude observed in the RANS heat flux results is higher. This might be related to the specific flight conditions leading to maximum thermal loads for flight point 2. The maximum heat flux of 388 kW/m² is reached at 76 % semi-span, while at 90 % the heat flux decreases to 296 kW/m². The slight shift of the maximum heat flux position might be related to the changes of Mach number and angle of attack. While a decrease in Mach number, here only from Ma 11 to Ma 10, would move the region of SSI in outward direction, a decrease in angle of attack, here from 40° to 30°, reduces the bluntness of the geometry and thus should move the region of SSI more inward. Similar to flight point 1, the empirical relationship is underpredicting the outboard heat flux, but now the maximum relative difference at 91 % semi-span increases to 21 %. For the HOTSOSE results the maximum relative overprediction of 10 % occurs at 86 % semi-span.

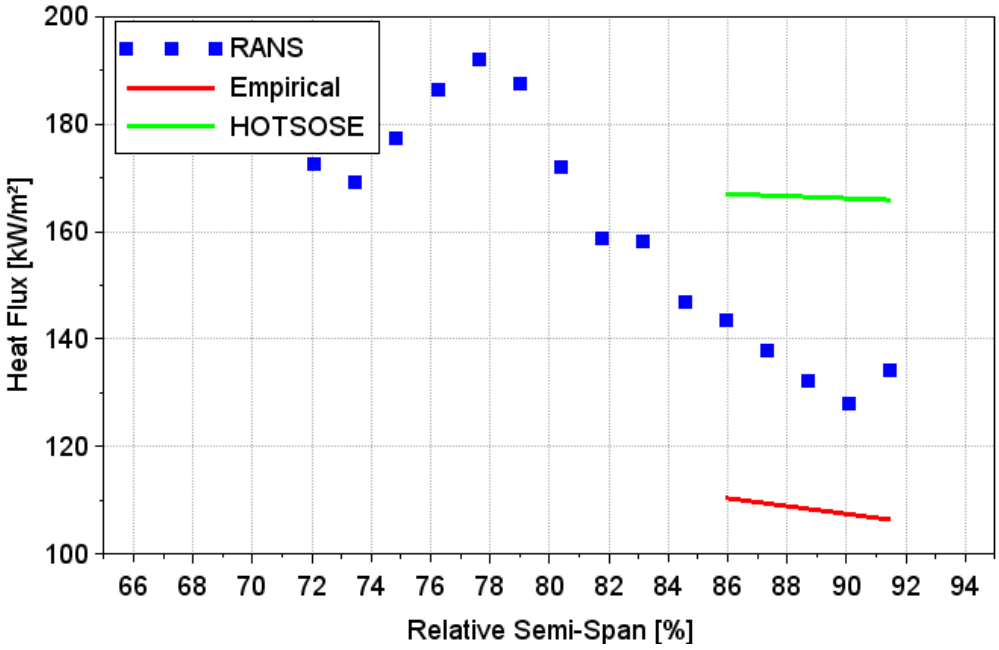

Fig 16. Heat flux evolution at FP 3 (Ma=7 / AoA=30° / Alt=45 km)

The RANS results for flight point 3 are shown in Fig 16. A maximum heat flux value of 192 kW/m² can be observed, while the value at 90 % semi-span is 128 kW/m². Similar to flight point 1 this yields a heat flux ratio of 1.5. The maximum is again reached at 78 % semi-span, which now might be due to a decrease in Mach number from 10 to 7 (the angle of attack stays constant). Different from flight points 1 and 2, there is a more pronounced decrease of heat flux from its peak value towards the outer leading-edge. Similar to flight points 1 and 2 empirical results underpredict and HOTSOSE overpredicts the heat flux as compared to the RANS results. The maximum relative differences as compared to the RANS results are 23 % and 24 %.

5. Summary and Conclusions

In the frame of the presented work the effect of shock-shock interference on the heat flux along the leading-edge of the SpaceLiner booster wing is analyzed. Based on defined ascent and descent trajectories the evolution of surface temperature in the area of the wing leading-edge is estimated. The estimation is based on one-dimensional heat conduction, the assumption of a generic CMC material and an empirical leading-edge heat flux relationship. Inviscid and RANS CFD are performed and deliver results for aerodynamic coefficients and the flow field around the SpaceLiner booster stage. The heat flux distribution is analyzed through RANS calculations performed for equilibrium air and considering high temperature effects. An isothermal wall is assumed for the RANS calculations that are performed for three flight points defined along the descent trajectory and located close to the peaks of thermal loads. The calculations for each flight point are performed for two wall temperatures. Like this a heat flux gradient can be determined and the obtained results can be adapted to the surface temperatures estimated previously.

For the defined flight points peak leading-edge heat fluxes in the area of SSI are determined by RANS to be 200 kW/m², 388 kW/m² and 192 kW/m² respectively. The peak heat fluxes for all three flight points occur at relative semi-span locations of 76 % to 78 %, a significant shift cannot be observed, although the changes might be attributed to variations of Mach number and angle of attack. When peak heat fluxes are compared to the heat flux in the area of the outer wing leading-edge at 90 % semi-span, ratios of 1.3 to 1.5 are obtained. The heat flux outside the region of SSI is also calculated with the empirical relationship used to determine the surface temperature and the DLR in-house aerothermodynamics tool HOTSOSE. For all three flight points the empirical relationship tends to underpredict the heat flux as compared to RANS results while the level of HOTSOSE results tends to be above the RANS values. Relative differences mostly stay within 10 % to 20 %, though.

The main conclusion resulting from the presented analysis is related to the question whether a fixed wing design is a viable option for the SpaceLiner configuration first stage despite of the shock-shock interference occurring in the area of the outer wing leading-edge. Looking at the results of the viscous CFD calculations this can be confirmed. The RANS calculations performed in the frame of this work show that maximum heat fluxes in the area of shock-shock interference along the wing leading-edge do not surpass 400 kW/m², even at the flight point of peak thermal load. Heat flux amplification by SSI yields factors of 1.3 to 1.5 only. Finally, temperatures estimated by the one-dimensional transient heat conduction approach are not going above 800 K which is in contrast to leading-edge temperatures used so far for the SpaceLiner booster TPS design, [17]. These significantly higher temperatures have been obtained by assuming radiation adiabatic equilibrium, which is known to be a conservative approach that in the case of the SpaceLiner booster stage is neglecting the highly transient evolution of the heat flux along the trajectory as shown in Fig 5 and Fig 6. So far, for high temperature regions ceramic materials including CMC have been foreseen within the thermal protection system design of the SpaceLiner booster stage, [17]. In agreement with that, a generic CMC material was as well used for surface temperature estimation in the area of the SpaceLiner booster wing leading-edge in the frame of the presented analysis. Of course, there is a number of simplifying assumptions done in the frame of the temperature estimation, as e.g. the assumption of a semi-infinite body. Also, flow fields determined by CFD in the frame of this work are either for ideal or equilibrium air while the real flight conditions might lead to a certain degree of nonequilibrium. However, even with the presence of SSI neither temperatures nor the heat fluxes in the area of the SpaceLiner booster wing leading-edge seem to be problematic from the point of view of the current booster TPS design. Thus, a fixed wing design should continue to be the baseline solution for the SpaceLiner booster stage.

References

1. Sippel, M., Schwanekamp, T.: The SpaceLiner Hypersonic System – Aerothermodynamic Requirements and Design Process, 8th European Symposium on Aerothermodynamics for Space Vehicles, Lisbon 2015
2. Sippel, M., Bussler, L., Kopp A. et al.: Advanced Simulations of Reusable Hypersonic Rocket-Powered Stages, 21st AIAA Spaceplanes Conference, Xiamen 2017
3. Sippel, M., Schwanekamp, T. et al.: SpaceLiner Technical Progress and Mission Definition, 20th AIAA Spaceplanes, Glasgow 2015
4. Sippel, M., Stappert, S., Bayrak, Y.M., Bussler, L., Callsen, S.: Systematic Assessment of SpaceLiner Passenger Cabin Emergency Separation Using Multi-Body Simulations, 2nd HiSST-Conference, Bruges, September 2022
5. Sippel, M., Stappert, S., Bussler, L., Forbes-Spyratos, S.: Technical Progress of Multiple-Mission Reusable Launch Vehicle SpaceLiner, HiSST 2018-1580839, 1st HiSST: International Conference on High-Speed Vehicle Science Technology, Moscow, November 2018
6. Sippel, M., Stappert, S., Bussler, L., Singh, S., Krummen, S.: Ultra-Fast Passenger Transport Options Enabled by Reusable Launch Vehicles, FAR Conference, Monopoli, 2019
7. Wilken, J., Bussler, L.: SpaceLiner System Specification Document, SL-SS-SART-0026-1/0, SART TN-001/2017
8. Bussler, L., Sippel, M., Kopp, A.: Reference Configurations AKIRA, SART TN-010/2017
9. Han, J.C.: Analytical Heat Transfer, CRC Press, 2012
10. Brandt, R., Frieß, M., Neuer, G.: Thermal Conductivity and Emissivity of Ceramic Matrix Composites at High Temperatures, High-Temperatures-High-Pressures, 2003/2004, vol. 35/36, pp. 169-177
11. Cunningham, J.A. et al.: Space Shuttle Wing Leading Edge Heating Environment Prediction Derived from Development Flight Data, Shuttle Performance: Lessons Learned (Part 2), NASA Langley Research Center, October 1983
12. Kayal, H.: Aufbau eines vereinfachten Simulationsmodells für den Bahnaufstieg in der Großkreisebene, DLR IB 318-93/05, DLR Cologne 1993
13. Langer, S., Schwöppe, A., and Kroll, N.: The DLR Flow Solver TAU—Status and Recent Algorithmic Developments, AIAA Paper 2014-0080, 2014
14. Spalart, P.R., and Allmaras, S.R., A One-Equation Turbulence Model for Aerodynamic Flows, AIAA Paper 1992-0439, 1992.
15. Capitelli, Colonna, Giordano, Maraffa, Casavola, Minelli, Pagano, Pietanza, Taccogna: Tables of Internal Partition Functions and Thermodynamic Properties of High-Temperature Mars-Atmosphere Species from 50K to 50000K, ESA STR-246, October 2005
16. Reisch, U., Streit, T.: Surface Inclination and Heat Transfer Methods for Reacting Hypersonic Flow in Thermochemical Equilibrium, DLR IB 129-96/10, DLR Braunschweig 1996
17. Schwanekamp, T., Garbers, N., Sippel, M.: Conceptual Design of the SpaceLiner Thermal Protection System, 8th European Symposium on Aerothermodynamics for Space Vehicles, Lisbon 2015